Physics-based tests to identify the accuracy of solar wind ion measurements: A case study with the Wind Faraday Cups

J. C. Kasper,[1] A. J. Lazarus,[1] J. T. Steinberg,[2] K. W. Ogilvie,[3] and A. Szabo[3]

Received 22 September 2005; revised 17 November 2005; accepted 16 December 2005; published 24 March 2006.

[1] We present techniques for comparing measurements of velocity, temperature, and density with constraints imposed by the plasma physics of magnetized bi-Maxwellian ions. Deviations from these physics-based constraints are interpreted as arising from measurement errors. Two million ion spectra from the Solar Wind Experiment Faraday Cup instruments on the Wind spacecraft are used as a case study. The accuracy of velocity measurements is determined by the fact that differential flow between hydrogen and helium should be aligned with the ambient magnetic field. Modeling the breakdown of field alignment suggests velocity uncertainties are less than 0.16% in magnitude and 3° in direction. Temperature uncertainty is found by examining the distribution of observed temperature anisotropies in high-beta solar wind intervals where the firehose, mirror, and cyclotron microinstabilities should drive the distribution to isotropy. The presence of a finite anisotropy at high beta suggests overall temperature uncertainties of 8%. Hydrogen and helium number densities are compared with the electron density inferred from observations of the local electron plasma frequency as a function of solar wind speed and year. We find that after accounting for the contribution of minor ions, the results are consistent with a systematic offset between the two instruments of 3–4%. The temperature and density methods are sensitive to non-Maxwellian features such as heat flux and proton beams and as a result are more suited to slow solar wind where these features are rare. These procedures are of general use in identifying the accuracy of observations from any solar wind ion instrument.

Citation: Kasper, J. C., A. J. Lazarus, J. T. Steinberg, K. W. Ogilvie, and A. Szabo (2006), Physics-based tests to identify the accuracy of solar wind ion measurements: A case study with the Wind Faraday Cups, *J. Geophys. Res.*, *111*, A03105, doi:10.1029/2005JA011442.

1. Introduction

[2] How can the accuracy of in situ solar wind ion measurements be determined after a spacecraft is launched? Laboratory testing provides a baseline for performance but cannot account for the effects of launch and the degradation of instrument response over the duration of a mission. In some cases, internal calibration systems exist to monitor the performance of critical components of instruments in flight. These calibration systems are effective in identifying drifts in instrument response but may not provide information on the accuracy of derived parameters such as velocities, temperatures, and densities. A common practice is the ''intercalibration'' of multiple instruments through statistical comparisons of measurements of the same parameters [*Petrinec and Russell*, 1993; *Paularena and Lazarus*, 1994]. Intercalibration, often performed with instruments on different spacecraft, suffers from the effects of real spatial and temporal variation of solar wind structures. Since it is often not clear which instrument is fundamentally more accurate, intercalibration is primarily useful for providing consistency across independent datasets, identifying deviation in the response of one or another instrument under particular circumstances, and for studying the real nonhomogeneity of the interplanetary medium [*King and Papitashvili*, 2005].

[3] A quantitative understanding of the accuracy of ion measurements is important for studies of the physics of the interplanetary medium. Our ability to study fundamental physical processes such as instabilities, dissipation, shocks, acceleration, and turbulence is limited by the reliability of our determinations of temperature anisotropies, Mach numbers, compression ratios, and velocity fluctuations. In addition, because solar wind measurements upstream of the Earth serve as input to geospace simulations, it is important to separate measurement errors from spatial structure when evaluating the terrestrial response to the solar wind.

[4] The purpose of this paper is to compare measurements of velocity, temperature, and density with constraints imposed by plasma physics considerations; we will interpret deviations from these physics-based constraints as arising from Gaussian-distributed measurement errors and identify the corresponding one-sigma uncertainties. The accuracy of

[1] MIT Kavli Institute for Astrophysics and Space Research, Massachusetts Institute of Technology, Cambridge, Massachusetts, USA.
[2] Los Alamos National Laboratory, Los Alamos, New Mexico, USA.
[3] NASA Goddard Space Flight Center, Greenbelt, Maryland, USA.

0148-0227/06/2005JA011442$09.00

ion velocities is determined by examining the alignment of differential flows between hydrogen and helium with the ambient magnetic field. The accuracy of ion temperature measurements is determined by tracking the range of observed temperature anisotropies in the limit of strong firehose and cyclotron plasma instabilities. Finally, the accuracy of ion densities is determined by comparing the electron number density implied by the ion densities with that determined by simultaneous observations of oscillations at the local electron plasma frequency. The procedures presented in this paper are of general use and are applicable to observations from any solar wind ion instrument.

[5] The power of the techniques presented herein is that each method is based on the statistical analysis of a large set of observations taken under a broad range of plasma conditions. In this paper, measurements collected by instruments on the Wind spacecraft are used as a case study to demonstrate the methods. The array of plasma instruments on Wind provides an ideal data set, with a decade of observations of thermal plasma, magnetic field, and electromagnetic waves in the interplanetary and geospace environments. Launched in October 1994, a combination of orbital maneuvers and lunar gravitational assists have sent Wind to the solar wind upstream of the Earth's bow shock, the distant geomagnetic tail, the lunar wake, and the first and second Lagrangian points located 1.5 million kilometers upstream and downstream, respectively, from the Earth along the Sun-Earth line. The Faraday Cup (FC) instruments on Wind, which are the focus of this study, have recorded over 2.5 million spectra of hydrogen and helium to date.

[6] The paper is organized as follows. In section 2, we describe the instruments used on the Wind spacecraft for this case study. Velocities are studied in section 3 and a comparison between observations and Monte Carlo simulations is consistent with an uncertainty in the speed of 0.16% and a maximum uncertainty in the direction of 3°. In section 4, we place a limit on the uncertainty in nonlinear and moment-derived temperatures and find an uncertainty in nonlinear temperatures of 8% and in moment temperatures of 15%. In section 5, we compare density measurements with WAVES/TNR observations of the electron plasma frequency and identify a systematic offset of 3% and a measurement uncertainty of 3%. A review of the FC instrument and a description of the two algorithms used to determine solar wind parameters is presented in Appendix A. Appendix B is a discussion of the overall stability of the FC instrument over time based on an internal calibration system.

2. Instruments

[7] The two Faraday Cup (FC) ion instruments of the Solar Wind Experiment (SWE) provide measurements of the kinetic properties of the hydrogen and helium ions that constitute the bulk of the solar wind [*Ogilvie et al.*, 1995]. The Wind satellite rotates with its spin-axis normal to the ecliptic plane. One FC points 15° southward out of the ecliptic plane; the second FC points 15° northward. Each FC measurement spectrum takes approximately 92 s to record. The hydrogen and helium parameters (herein denoted with the subscripts p and α) derived from FC spectra for this study are based on a characterization of the solar wind velocity distributions with the convected bi-Maxwellian function. For each species $j = p, \alpha$ with number density n_j, bulk velocity $\vec{v}$, separate most probable thermal speeds $w_{\|j}$ and $w_{\perp j}$ parallel and perpendicular to the ambient field $\vec{B}$, the distribution $f_j(\vec{v})$ takes the form,

$$f_j(\vec{v}) = \frac{n_j}{\pi^{3/2} w_{\perp j}^2 w_{\|j}} \exp\left(-\left[v_\perp^2/w_{\perp j}^2 + v_\|^2/w_{\|j}^2\right]\right), \quad (1)$$

where $v_\perp$ and $v_\|$ are the components of $\vec{v} - \vec{V}_j$ perpendicular and parallel to the direction $\hat{b}$ of the ambient magnetic field,

$$v_\| = (\vec{v} - \vec{V}_j) \cdot \hat{b}, \quad \vec{v}_\perp = \vec{v} - v_\| \hat{b}. \quad (2)$$

The most probable thermal speeds are related to the corresponding temperatures by $k_B T_{\perp j} = {}^1/_2 m_j w_{\perp j}^2$ and $k_B T_{\|j} = {}^1/_2 m_j w_{\|j}^2$, where m_j is the mass of the species and k_B is Boltzmann's constant. The algorithms used for extracting hydrogen and helium velocity, temperature, and density are outlined in Appendix A. The FC dataset is available for public use at the National Space Science Data Center (NSSDC) (http://nssdc.gsfc.nasa.gov).

[8] Measurements of the vector magnetic field were obtained from the Wind Magnetic Field Investigation (MFI), which consists of boom-mounted, dual, triaxial fluxgate magnetometers [*Lepping et al.*, 1995]. Individual vector measurements are telemetered at a rate of at least 10.9 vectors per second. In this study we began with 3-s vector magnetic field measurements obtained by averaging over the spin period of the spacecraft. These 3-s vector field measurements are also available at the NSSDC. For each 92-s FC spectrum, the corresponding set of 3-s MFI measurements were identified and the average magnetic field $\vec{B}_o$, field direction $\hat{b}$, and angular variation of $\hat{b}$ were calculated.

[9] The Thermal Noise Receiver (TNR) instrument in the WAVES experiment measures the power of electromagnetic fluctuations at a cadence of 0.2–4.5 s in the frequency range from 4 to 300 KHz [*Bougeret et al.*, 1995]. The solar wind plasma fluctuates at the electron plasma frequency, a quantity that is a function of the local electron number density only and varies from 50 to 300 KHz under typical solar wind conditions. The details of the spectrum of thermal fluctuations near the electron plasma frequency may be used to derive parameters such as the local electron number density and temperature [*Meyer-Vernet and Perche*, 1989; *Maksimovic et al.*, 1995]. An analysis of TNR power spectra made available by the Centre de Données de la Physique des Plasmas (CDPP) (http://cdpp.cesr.fr) provided the electron plasma frequency and in turn the electron number density at a typical cadence of 6 s. The TNR measurements were then averaged over the 92-s FC spectrum accumulation time.

3. Velocities and Field-Aligned Differential Flow

[10] Helium and minor ions generally flow faster than hydrogen, especially in the fast solar wind [*McKenzie et al.*, 1978; *Marsch et al.*, 1982a, 1982b; *von Steiger et al.*, 1995]. This phenomenon is generally believed to be an artifact of

wave-resonant heating and acceleration in the corona [e.g., *Dusenbery and Hollweg*, 1981; *Tu et al.*, 2003]. The maximum values of the differential flow are typically of the order of the local Alfvén speed, and this has been attributed to the limiting action of local plasma microinstabilities [*Xing and Habbal*, 2000; *Araneda et al.*, 2002]. The magnitude of the differential flow is observed to decrease with radial distance from the Sun, in part due to Coulomb drag between the species [*Neubauer*, 1976], but flows of up to 10% of the bulk speed are commonly observed at 1 AU. Wind observations of differential flow between hydrogen and helium have been reported previously [*Steinberg et al.*, 1996]. The broad range of observed differential flow speeds can be used in combination with magnetic field measurements to place an upper limit on the uncertainty of the ion velocity measurements. We define the differential flow vector of the helium relative to the hydrogen,

$$\Delta\vec{V}_{\alpha p} \equiv \vec{V}_{\alpha} - \vec{V}_{p}. \tag{3}$$

[11] Regardless of the magnitude of $\Delta V_{\alpha p}$, the interplanetary magnetic field will restrict the direction of a finite differential flow. A component of $\Delta\vec{V}_{\alpha p}$ perpendicular to $\vec{B}_o$ would lead to a net force that would result in a gyrotropic distribution within several cyclotron periods, a timescale of seconds in the interplanetary medium. Thus in the absence of sudden transients such as interplanetary shocks or strong fluctuations of the field $\Delta\vec{V}_{\alpha p}$ must always be either parallel or antiparallel to $\vec{B}_o$. Define θ_{BV} to be the acute angle between the measured differential flow and magnetic field vector,

$$\theta_{BV} = \cos^{-1}\frac{|\Delta\vec{V}_{\alpha p}\cdot\vec{B}_o|}{\Delta V_{\alpha p}B_o} \tag{4}$$

[12] Any measured departure of θ_{BV} from zero is a combination of measurement errors and fluctuations in the $\vec{V}_p$, $\vec{V}_{\alpha}$, and $\vec{B}_o$ vectors over the course of the observation. Consider the variation of θ_{BV} due to measurement uncertainties as a function of the magnitude of the differential flow relative to the bulk proton speed, $\Delta V_{\alpha p}/V_p$. When $\Delta V_{\alpha p}$ is much smaller than the uncertainty in the measurements of either V_p or V_{α}, then $\Delta V_{\alpha p}/V_p$ will appear to have a random orientation relative to $\vec{B}_o$ and there will be a large observed spread in θ_{BV} from 0° to 90°. On the other hand, when $\Delta V_{\alpha p}$ is much larger than the uncertainty in the measurements of the bulk velocity we would expect the measured values of θ_{BV} to cluster close to 0°, with any spread due to real fluctuations in the parameters over the course of the measurement and any misalignment between the instruments. By examining the rate at which the observed distribution of θ_{BV} spreads out as $\Delta V_{\alpha p}/V_p$ decreases, we can place a limit on the accuracy of the velocity measurements.

[13] In the bi-Maxwellian analysis of the SWE Faraday Cup measurements, each species, proton and alpha, was separately fit with a vector velocity, and no assumption was made about alignment of the differential flow with the field. The average value of $\vec{B}_o$ was based on the 3-s MFI data recorded during the FC spectrum. In Figure 1, we show the distribution of solar wind observations as a function of cos θ_{BV} and $\Delta V_{\alpha p}/V_p$ as a two-dimensional histogram. The

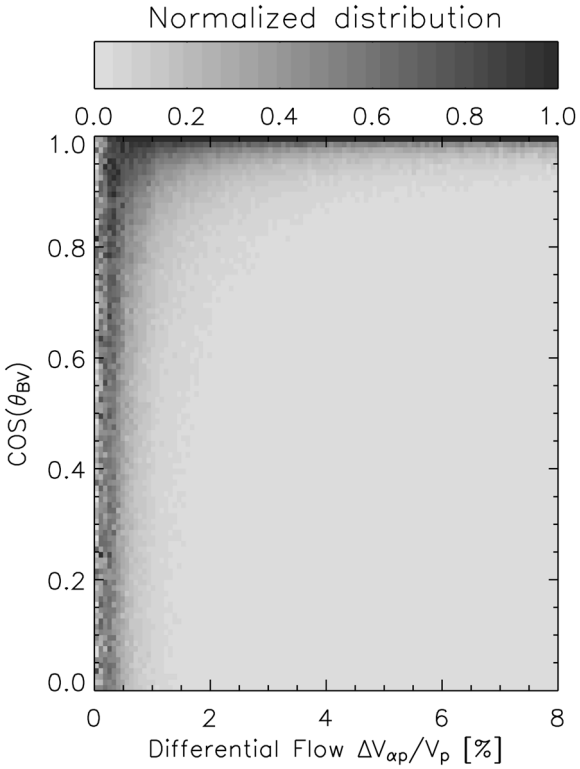

Figure 1. The distribution of ion measurements as a function of the fractional differential flow speed, $\Delta V_{\alpha p}/V_p$, and the acute angle, θ_{BV} between the differential flow and the average magnetic field. The total number of measurements in each vertical column has been normalized to unity to remove the overall distribution of measurements with differential flow. For large differential flows with $\Delta V_{\alpha p}/V_p >$ 3% the differential flow vector is closely aligned with the ambient magnetic field. For small values of $\Delta V_{\alpha p}/V_p$ the velocity difference between the two ion species is comparable to the uncertainty of the velocity measurements and the distribution of θ_{BV} becomes isotropic.

qualitative features of this histogram are in agreement with our predictions. For large values of the differential flow, the measurements are tightly clustered within several degrees of the magnetic field, or cos θ_{BV} = 1. As the measured flow decreases below $\Delta V_{\alpha p}/V_p$ of two percent, the range of angles begins to spread rapidly, and below half a percent, the distribution is nearly isotropic.

[14] Presumably, the spread in Figure 1 implies that the uncertainty in the velocities is on the order of a percent. As we shall now demonstrate, a simple numerical simulation can reproduce the observed distribution of cos θ_{BV} and allow us to identify the sources of the error. In order to compare these observations with simulations we define a critical angle θ_c that quantifies the breakdown of field alignment. Figure 2 is a series of histograms of θ_{BV}, that are essentially vertical slices of Figure 1, for several values of $\Delta V_{\alpha p}/V_p$ starting at 0.5% and increasing in 0.75% increments. We find that the distribution of the number of measurements, N, with θ_{BV} can be described by an exponential relation, namely,

$$N = A\exp(B\cos\theta_{BV}), \tag{5}$$

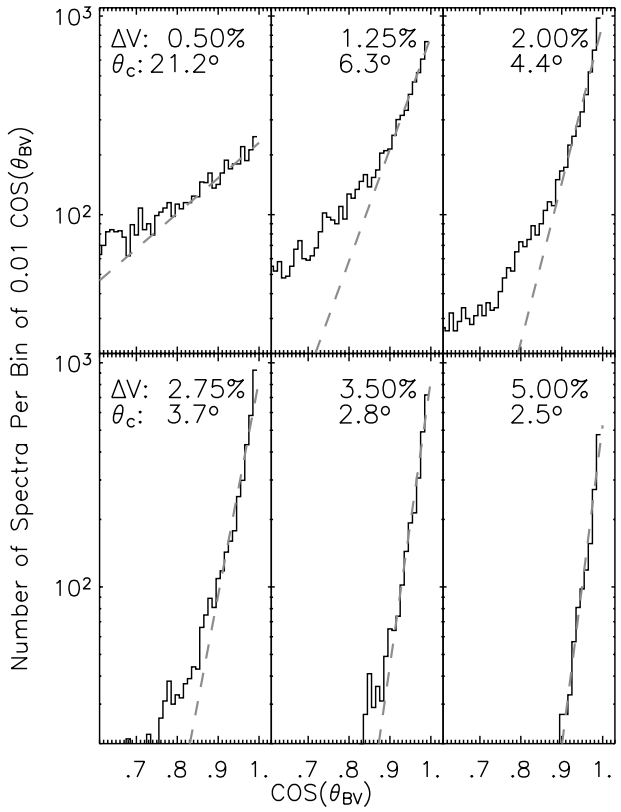

Figure 2. The distribution of observations as a function of cos θ_{BV} for six intervals in $\Delta V_{\alpha p}/V_p$ between 0.5% and 5%. The dashed lines are the best-fit exponential curves to the observed distributions. The values of the best-fit are used to determine the critical angle θ_c where the histogram falls to 99% of the peak at $\theta_{BV} = 0°$. For $\Delta V_{\alpha p}/V_p$ greater than 5%, θ_c is less than 2.5°, demonstrating the alignment between the FC velocities and the magnetic field.

where A and B are free parameters. Here, θ_c is defined as the angle, for a specified interval of $\Delta V_{\alpha p}/V_p$, where the number of spectra falls to 1% of the value at $\theta_{BV} = 0°$. By substituting θ_c into equation (5) and using Ae^B for the number of observations at $\theta_{BV} = 0°$, one can solve for the critical angle,

$$\theta_c \equiv \cos^{-1}\left(1 + B^{-1}\ln 10^{-2}\right). \tag{6}$$

The best fit of (5) to the observations is shown as a gray dashed line in each panel of Figure 2, with the resulting value for θ_c supplied in the upper left corner. For differential flow greater than 5% of the bulk proton speed, 99% of the FC measurements are aligned within 2.5° of the direction of the interplanetary magnetic field.

[15] The accuracy of the velocity measurements can be quantified further by comparing the observed θ_c with Monte Carlo simulations. We find that the variation of θ_c can be reproduced assuming there are two sources of error, a percentage uncertainty in the magnitude of the ion speeds σ_V and an angular error σ_θ that represents both measurement errors and real fluctuations in the flow and field over the duration of the FC measurement. In the following discussion of the simulation, the matrix operator $\mathbf{R}(\alpha)$ rotates a vector by the angle α in a random direction. Random numbers indicated by η are uniformly distributed from [0, 1] and those by $\xi[x]$ are Gaussian distributed with a standard deviation of x.

[16] We begin by selecting a proton solar wind speed uniformly between 300 and 600 km/s and rotating randomly by 5° about the radial direction,

$$\vec{V}_p = 300(1+\eta)\mathbf{R}(\xi[5°])\hat{r}, \tag{7}$$

where $\hat{r}$ is a radial unit vector. A value for $\Delta V_{\alpha p}$ is then selected between 0 and 10% of V_p,

$$\Delta V_{\alpha p} = (0.1\eta)V_p. \tag{8}$$

These simple rules for bulk speed and differential flow were used because more realistic distributions did not noticeably affect the outcome of the simulations. In contrast, the distribution of the direction of the field is important, so $\hat{b}$ is drawn from the distribution of Wind observations shown in Figure A2a in Appendix A. The helium vector velocity is then determined,

$$\vec{V}_\alpha = \vec{V}_p + \hat{b}\Delta V_{\alpha p}. \tag{9}$$

Any angular error and angular fluctuation is then captured in a rotation of the magnetic field direction by a characteristic angle σ_θ to produce the "measured" direction,

$$\hat{b}' = \mathbf{R}(\xi[\sigma_\theta])\hat{b}. \tag{10}$$

We found that random rotations of the field and a systematic angular shift between the ion and field measurements were found to produce the same result. The "measured" velocities are then determined by adding on a fractional error σ_V to the each component of $\vec{v}_\alpha$ and $\vec{v}_p$,

$$V'_{jk} = V_{jk}(1 + \xi\sigma_V), \tag{11}$$

where j is the species and k is the component of the velocity. Finally, we calculate the angle θ'_{BV}

$$\theta'_{BV} = \cos^{-1}\frac{\left|\left(\vec{V}'_\alpha - \vec{V}'_p\right)\cdot\hat{b}'\right|}{\left|\vec{V}'_\alpha - \vec{V}'_p\right|}. \tag{12}$$

For each simulation, values of σ_V and σ_θ were selected and one million synthesized measurements were generated. We then followed the same routine outlined above to determine the critical angles θ'_c. Figure 3 compares the variation of θ_c and θ'_c as a function of $\Delta V_{\alpha p}/V_p$ and selected values of σ_V and σ_θ. The diamonds are the measured values of θ_c determined for all differential flows, including the selected intervals shown in Figure 2. The dark lines were generated from a series of runs with $\{\sigma_\theta = (4°, 6°, 8°, 10°), \sigma_V = 0\%\}$. The angular error is sufficient to reproduce the asymptotic values of θ_c with large $\Delta V_{\alpha p}/V_p$ but does not generate the rapid increase in θ_c with small differential flow. The gray dashed lines are runs with $\{\sigma_\theta = 0°, \sigma_V = (0.1\%, 0.15\%, 0.2\%, 0.25\%)\}$. A finite value for σ_V reproduces the

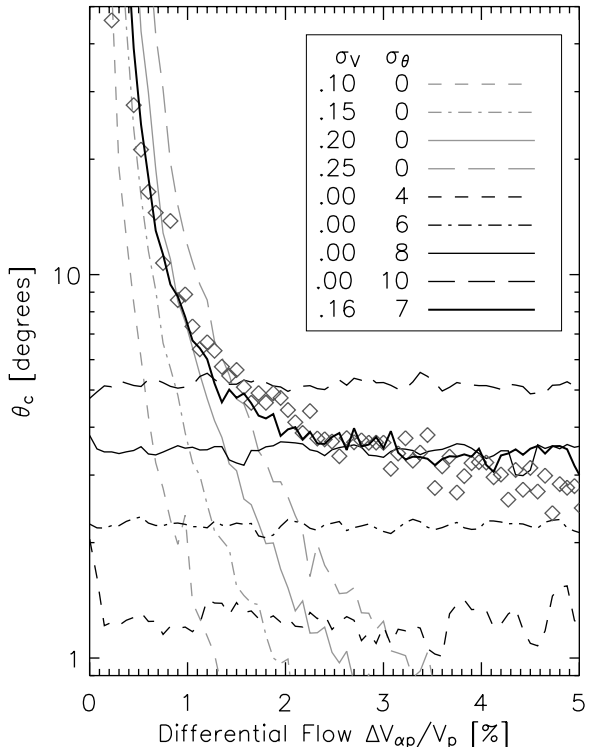

Figure 3. Comparison of the observed variation of θ_c (diamonds) as a function of $\Delta V_{\alpha p}/V_p$ with simulations (lines). The dashed gray lines represent different values for the uncertainty in the bulk speed from 0.1% to 0.25%. The dashed black lines are for different values of angular uncertainty from 4° to 10°. The simulation that best reproduced the observed variation of θ_c combined a speed uncertainty of 0.16% with an angular uncertainty of 7°, at least 4.5% of which is attributed to the angular variation of the magnetic field over 92 s.

observed behavior for small flows. The simulation that resulted in the best overall agreement with the observations was with $\sigma_\theta = 7°$, $\sigma_V = 0.16\%$. The error estimate is a combination of flow angle uncertainties and fluctuations in the magnetic field over the course of a spectrum.

[17] On average, the typical angular variation of $\vec{B}_o$ using the 3-s MFI data was 4.5°. If the errors are linearly independent, then they add in quadrature and the uncertainty in the flow angle must be no more than about 3°. This flow angle uncertainty is much larger than the average error estimate from the nonlinear fitting presented in Appendix A and illustrates the value of these quantitative tests.

[18] Several comments are in order. We commonly use alignment between the differential flow and the field as a consistency check to ensure that the software fit the alpha distribution and not, for example, a proton beam. This check is clearly only valid for differential flows greater than a few percent. The remarkable alignment between the differential flow and the field, with 99% of the FC measurements aligned within 2.5° of the field direction determined with MFI, suggests two improvements to the Wind SWE data analysis. First, a scalar differential flow between the hydrogen and the helium can be used, in combination with the field direction and the proton velocity, instead of an independent vector velocity for the helium. This process would remove two degrees of freedom from the nonlinear fitting and significantly improve the stability and robustness of the analysis. Second, we could use the 3-s vector field for each spin of the spacecraft when calculating the instrument response instead of an average field over the duration of the spectrum.

4. Temperatures and Their Anisotropies

[19] Measurements in the solar wind and magnetosheath have demonstrated that the observed range in proton temperature anisotropy,

$$R_p \equiv \frac{T_{\perp p}}{T_{\parallel p}}, \tag{13}$$

decreases sharply with increasing parallel proton plasma beta, $\beta_{\parallel p} = n_p k_B T_{\parallel p}/(B^2/2\mu_o)$. Observations and theoretical work discussed below have shown that R_p is bounded by the effects of plasma microinstabilities driven by the proton temperature anisotropy. In a collisionless electron-proton plasma where the thermal proton velocity distribution may be approximated as a bi-Maxwellian, the mirror and cyclotron instabilities limit the anisotropy when $R_p > 1$, and the firehose instability limits it when $R_p < 1$. The firehose instability is a growing mode, which has a real frequency ω_r and satisfies $\omega_r < \Omega_p$ where Ω_p is the proton cyclotron frequency [*Parker*, 1958]. *Gary et al.* [1998] showed that under resonant conditions the linear threshold condition for a fixed value of the dimensionless maximum growth rate γ_m/Ω_p of this instability in an electron-proton plasma can be written for $\gamma_m/\Omega_p < 0.1$ as

$$R_{pf} = 1 - \frac{S_{pf}}{\beta_{\parallel p}^{\alpha_{pf}}} \tag{14}$$

over $1 \leq \beta_{\parallel p} \leq 10$ where S_{pf} and α_{pf} are fitting parameters. In the nonresonant long-wavelength limit, the firehose instability threshold corresponds to $S_{pf} = 2$ and $\alpha_{pf} = 1$. *Eviatar and Schulz* [1970] studied the firehose instability assuming a constant magnetic field for a limited data set of several hours measured by the Vela 4 spacecraft. A long-term statistical study of Wind FC observations by *Kasper et al.* [2002] conclusively demonstrated the presence of the firehose instability in the expanding solar wind plasma at 1 AU. We use the *Kasper et al.* [2002] results, with $S_{pf} = 1.03$ and $\alpha_{pf} = 0.54$. In the following discussion of the error in temperature measurements, the precise values for the limiting anisotropy imposed by the instabilities is much less important than the fact that the limits grow more stringent with increasing $\beta_{\parallel p}$.

[20] The electromagnetic proton cyclotron anisotropy instability is driven by $R_p > 1$ and has been studied extensively [see *Gary et al.*, 2000, and references therein]. The limit to R_p imposed by the cyclotron instability is predicted to take the form,

$$R_{pc} = 1 + \frac{S_{pc}}{\beta_{\parallel p}^{\alpha_{pc}}}. \tag{15}$$

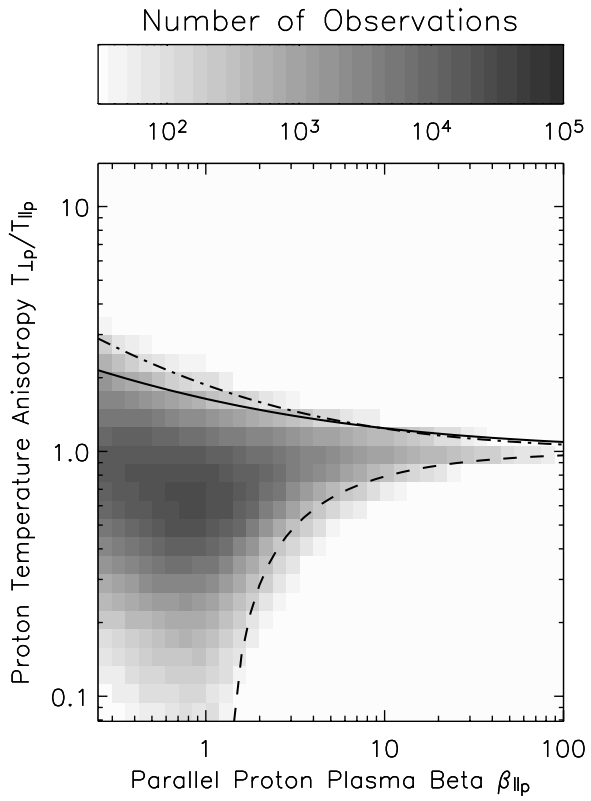

Figure 4. The two-dimensional distribution of solar wind proton measurements as a function of $\beta_{\|p}$ and $T_{\perp}p/T_{\|p}$. The shading indicates the number of observations in each bin as per the scale. The gray curves indicate the theoretical predictions for the bounds imposed on the proton temperature anisotropy by the firehose (dashed), cyclotron (solid), and mirror (dashed-dotted) instabilities. Note that as $\beta_{\|p}$ increases above two the observed range of $T_{\perp p}/T_{\|p}$ should continually decrease. The subsequent failure of the range of anisotropy to decrease can be used to estimate the uncertainty of the temperature measurements, as is shown in Figure 5.

This constraint has been verified through observations in the magnetosheath [*Phan et al.*, 1994; *Anderson et al.*, 1994; *Tan et al.*, 1998], in the outer magnetosphere [*Anderson et al.*, 1996], in the solar wind [*Gary et al.*, 2001], and in a laboratory experiment [*Scime et al.*, 2000]. Typical values for the free parameters in equation (15) are $S_{pc} = 0.64$ and $\alpha_{pc} = 0.42$. If $\beta_{\|p} > 10$, the mirror instability will also act to constrain the anisotropy for $R_p > 1$, but for our purposes it is sufficient to consider the cyclotron mode.

[21] The limiting effect of the instabilities is evident in Figure 4, which is a two-dimensional histogram of the distribution of 1 million solar wind spectra as a function of R_p and $\beta_{\|p}$ (an updated version of Figure 3 by *Kasper et al.* [2003]). Spectra with poor fits to a bi-Maxwellian, due for example to proton beams, are excluded from this distribution, resulting in a sample dominated by slow solar wind with speeds less than 450 km/s. Our analysis of proton beams has mainly focused on the lunar wake [*Clack et al.*, 2004], but an initial survey of 80,000 FC spectra in 1995 detected proton beams 10% of the time at 300 km/s, 25% at 450 km/s, and 50% at 500 km/s [*Clack et al.*, 2002]. The gray curves represent the upper bounds imposed on R_p by the cyclotron and mirror instabilities and the lower bound imposed by the firehose instability.

[22] As $\beta_{\|p}$ increases, the bounds imposed on R_p by the limits in equations (14) and (15) constrain the anisotropy to a diminishing region near unity. A finite measurement error in the two temperatures will also generate a spread in R_p. At some point $\beta_{\|p}$ will be large enough that the observed variation in R_p will be dominated by the uncertainty in the measurements, and we can relate the observed standard deviation of measurements to the uncertainty in the temperature measurements. By propagating the individual uncertainties in the perpendicular and parallel temperatures, $\sigma_{T\perp}$ and $\sigma_{T\|}$, we can derive the expected distribution of measurements of R_p,

$$\sigma_{Rp}^2 = \frac{\sigma_{T\|}^2}{T_{\|}^2} + \frac{T_{\perp}^2 \sigma_{T\|}^2}{T_{\|}^4} \approx 2\frac{\sigma_T^2}{T^2} \tag{16}$$

where in the final step we have assumed that for $R_p \rightarrow 1$, $T_{\perp p} = T_{\|p} = T$ and the two temperatures have the same uncertainty σ_T. In Appendix A we present evidence that the uncertainties of $T_{\perp p}$ and $T_{\|p}$ are each a function of the magnetic field direction (see Figure A2 in Appendix A). For the bulk of the measurements, with the magnetic field in the Parker field orientation, the uncertainties in the temperatures are approximately equal, so we feel this assumption is justified.

[23] The observations were divided into 35 intervals in $\beta_{\|p}$ spaced logarithmically between 10^{-3} and 10^2. For each interval, we calculated the standard deviation σ_{Rp} of both the moment and nonlinear measurements of R_p. In Figure 5, we plot σ_{Rp} as a function of $\beta_{\|p}$ for the moments (triangles) and nonlinear (diamonds) data sets. We also determined an expected value for σ_{Rp} by calculating the standard deviation of R_p if the observations were uniformly distributed between R_{pf} and R_{pc}. This predication is drawn as the solid line on the plot. For both the moment and nonlinear methods, σ_{Rp} eventually stabilizes to a value greater than that expected from the prediction. On the right axis, we show the inferred temperature uncertainty based on equation (16). For values of $\beta_{\|}p$ less than a few, the derived σ_{Rp} is smaller than the limits expected due to the instabilities alone and is a complex function of the real distribution of R_p due to the effects of instabilities, heating, expansion, and the general evolution of the solar wind from the corona to interplanetary space. For $\beta_{\|p} > 4$, σ_{Rp} is constant at about 0.2 for the moments (shown as the dashed line in Figure 5). This value of σ_{Rp} corresponds to an inferred temperature uncertainty of 15%. The nonlinear version of σ_{Rp} asymptotes to 0.1 for $\beta_{\|p} > 10$ (dotted line), or approximately 8% for the corresponding temperature uncertainty. This result is in agreement both with the average derived uncertainties in the temperatures from the nonlinear fits and with the typical deviation between the moment and nonlinear values shown in Table A1 in Appendix A.

[24] We have shown that the persistence of a finite variation in temperature anisotropy at high $\beta_{\|}p$ may be used to estimate the uncertainty in temperature measurements. Several assumptions went into this procedure,

including that the parallel and perpendicular temperatures had the same error and that the uncertainties were not functions of other solar wind parameters such as speed, density, or $\beta_{\|p}$. As far as we are aware, this is a unique and novel technique for identifying the error in temperature measurements. The 8% uncertainty in temperature is useful to know for the calculation of shock parameters or when testing a structure for pressure balance. Additionally, these results have implications for studies of instabilities driven by temperature anisotropies. Clearly, studies of constraints to R_p based on instabilities should focus on regimes where the deviation of the temperatures from isotropy is greater than 10%. We also find that to the extent the solar wind can be described as a bi-Maxwellian, the nonlinear analysis that fits a model response function to measurements produces a more physically consistent temperature than the moment analysis. Further studies should try to identify the roles played by true measurement errors and by nonthermal features such as heat fluxes and proton beams in leading the higher errors in temperatures determined through moments.

5. Number Density

[25] Electrostatic oscillations at the local plasma frequency are common in the interplanetary medium and may be used to identify the local electron number density. Measurements of these waves have been used to calibrate electron instruments on Wind and Ulysses [*Salem et al.*, 2001; *Issautier et al.*, 2001]. The goal of this section is to compare the electron number density inferred from WAVES/TNR observations of the local electron plasma frequency with a value derived from the FC ion measurements. Variation in the measured number densities due to evolution in detectors and measurement electronics over the mission is discussed in Appendix B and is believed to be less than 0.2% over the last decade. Since hydrogen and helium are fully ionized in the solar wind, the total electron number density due to protons and alphas is $n_p + 2n_\alpha$. Among other factors, the relative abundance of helium is a function of solar wind speed and phase of the solar cycle, but during solar maximum n_α is 4.5% of n_p [*Aellig et al.*, 2001a]. If n_e is the total electron number density measured by TNR, and all of the measurements are exact, then the fractional excess, ε, of electrons is

$$\varepsilon = \left(n_e - n_p - 2n_\alpha\right)/n_e \tag{17}$$

[26] The excess ε is due to any systematic offset between the two instruments, measurement errors, and the contribution of minor ion species in the solar wind. A small fraction of the solar wind is composed of minor ions such as oxygen and iron. While their relative abundance is rather low, their rather high average charge states (e.g., oxygen $\sim 6^+ - 7^+$ and iron $\sim 8.5^+ - 10.5^+$ depending on the solar wind regime) make them more prominent contributors to the solar wind electron density. We estimated the contribution of minor ions to the total electron density in the solar wind for both interstream and coronal hole type solar wind. The analysis focused on the most prominent minor ions (ordered by mass): C, N, O, Ne, Mg, Si, S, and Fe. The abundances of the elements (except sulfur) were taken from a compilation by *von Steiger* [1995] for both types of solar wind. For the sulfur abundance in the coronal hole solar wind we use results reported by *Shafer et al.* [1993] while we assumed the same fractionation versus its photospheric value for sulfur as is observed for carbon in the slow solar wind (fractionation measured versus oxygen). The charge states of the minor ions analyzed were estimated based on abundance measurements by various instruments [*von Steiger*, 1995; *Hefti et al.*, 2000]. On the basis of the above assumptions on relative elemental and ionic abundances for minor ions, the minor ions are estimated to contribute $\varepsilon \sim 0.8\%$ of the total electron density in the interstream solar wind and $\varepsilon \sim 1.5\%$ in the coronal-hole type solar wind. We also verified these estimates by examining a data set of 1-hour averages of O, C, Ne, Mg, Si, and Fe abundance and charge state observed over 2004 by the Solar Wind Ion Composition Spectrometer (SWICS) on the Advanced Composition Explorer (ACE) (S. Lepri and J. Raines, private communication, 2005).

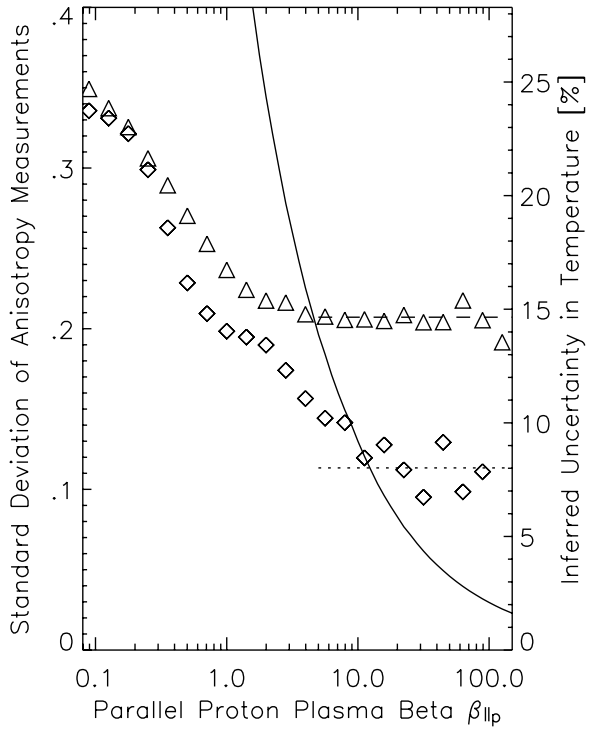

Figure 5. The standard deviation σ_{Rp} of the measured values of the proton temperature anisotropy $R_p = T_{\perp p}/T_{\|p}$ as a function of $\beta_{\|p}$ for the moment (triangles) and nonlinear (diamonds) methods. The solid line is a prediction of σ_{Rp} using simulated data uniformly distributed between the limits imposed by the firehose, cyclotron, and mirror instabilities. For $\beta_{\|p} > 3$, the moment values of σ_{Rp} asymptote to 0.2, and for $\beta_{\|p} > 10$, the nonlinear values of σ_{Rp} asymptote to 0.1. The corresponding uncertainty in temperature derived from equation (16) is shown on the right axis. These results suggests that the inferred uncertainty in proton temperatures is approximately 8% for the fits and 15% for the moments.

[27] We can separately identify the offset and measurement error of the density by calculating the average excess $\bar{\varepsilon}$ and the standard deviation σ_ε. A comparison of SWE/FC

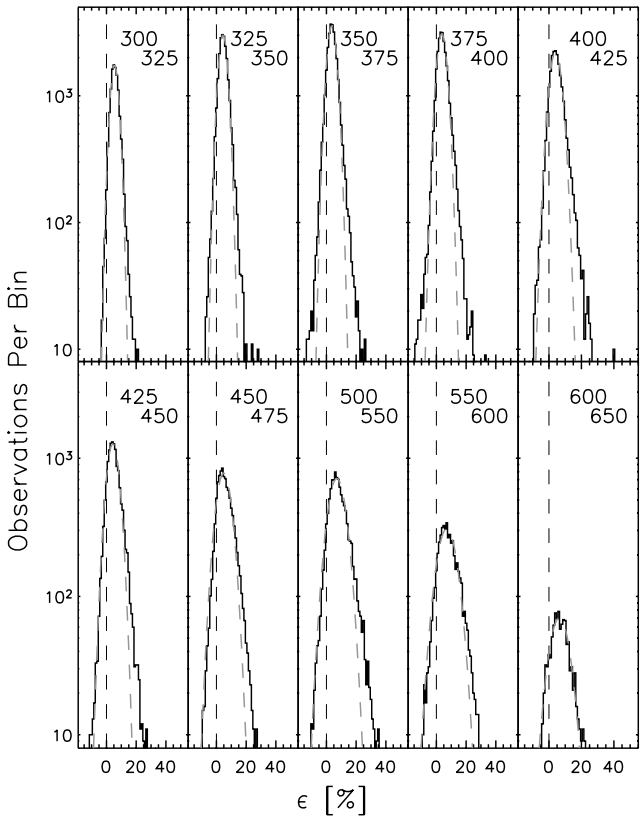

Figure 6. Histograms of ε, the calculated fractional excess of electrons in six speed windows using selected data in 1995. The speed range in km/s is indicated at the top of each panel. Each histogram is the number of spectra observed per 0.5% bin in ε. The dashed gray lines are the best fit of a Gaussian to the distribution and the dark vertical lines at ε = 0 are to guide the eye.

and WAVES/TNR observations, limited to 6 days in 1996, was reported previously [see *Maksimovic et al.*, 1998, Figure 2]. In that study $\bar{\varepsilon} \sim 1\%$ with a spread of $\sigma_\varepsilon = 4\%$. There are several compelling reasons to pursue this comparison in more detail. The analysis of the TNR data has been refined due to a better understanding of the antennae and the TNR frequency bins. In addition, 6 days are insufficient to probe possible dependencies on solar wind conditions, such as the bulk speed. In this section, we will extend the *Maksimovic et al.* [1998] results by studying $\bar{\varepsilon}$ and σ_ε as a function of the proton speed and time.

[28] This study uses all solar wind observations in the interval 1995–2000. Since the end goal is to produce as clear and confident a value for ε as possible, any measurements that seem at all suspicious are discarded. All TNR measurements occurring during each FC spectrum were identified and the average and standard deviation of n_e were calculated. Intervals with large variation in n_e within the spectrum, poor fits to the helium spectra, large values of χ^2, or fewer than ten corresponding TNR measurements were discarded. A total of 7×10^5 spectra, or one third of the mission, passed all of the cuts and were used for the study of ε. The median value of ε over the entire selected data set was 5.8%, with an average value of 6.3% and a standard deviation of 5.1%. The standard deviation is in agreement with the observations of *Maksimovic et al.* [1998], although ε is 4% larger than was reported in that study. This difference can be attributed in part to the refined analysis of the TNR data since that study and to the fact that on average the proton number densities derived from the bi-Maxwellian analysis are about 1% smaller than the Wind number densities which were used in that study. We believe that the 1% shift in the FC number densities is due to the use of new effective area and response functions.

[29] For each year, the selected observations were divided into ten intervals in speed ranging from 300 to 650 km/s. The first seven windows are 25 km/s wide and span from 300 to 475 km/s. Since the number of measurements decreases with speed, the final three windows are 50 km/s wide to improve the statistics of the high-speed intervals and cover the speed range from 500 to 650 km/s. The ten histograms of ε as a function of speed window for 1995 are shown in Figure 6. The dashed gray lines are the best fit of a Gaussian profile. Overall, the Gaussian fit describes the observed distributions well. Several trends are worthy of comment. First, note that in most cases the portion of each histogram with values of $\varepsilon < 0$, an unphysical result may be accounted for by the natural width σ_ε of the distributions. In other words if the σ_ε in part represent the overall uncertainty of ε then it is natural for this amount of observations to have $\varepsilon < 0$. Note as well that σ_ε increases as a function of speed. Additionally, there appears to be a bias, or tail in many of the distributions at high values of ε, suggesting that there are some intervals where ε is enhanced beyond the simple Gaussian variation observed.

[30] In Figure 7 we plot σ_ε and $\bar{\varepsilon}$ derived from the Gaussian fits as a function of speed. The shaded years printed along the top panel indicate the corresponding year of each profile. In general, σ_ε grew linearly from about 1.5% to 3% as the speed increased from 300 to 650 km/s. There is a suggestion of a time dependent increase in the width of the distributions in the speed range 375–475 km/s with solar cycle. In the lower panel of Figure 7, $\bar{\varepsilon}$ is plotted as a function of speed. Measurements in the same speed window have been offset by several km/s to reduce confusion. The horizontal error bars are the widths of the speed bins and the vertical error bars are the derived values of σ_ε . The grey region between 0.8 and 1.5% indicates the contribution to ε from minor ions, and the dashed line indicates overall typical value of $\bar{\varepsilon} = 5.4\%$. The differences are more than an order of magnitude larger than the variation of the instrument response as determined in Appendix B. There appears to be a two-state distribution in the interval $V_p <$ 425 km/s, with all observations in 1995–1997 and in 1998–2000 falling into two distinct intervals. For $V_p >$ 500 km/s ε is consistently greater then the predicted values. This high-speed property might reflect the fact that high-speed solar wind often contains two proton distributions, and this second proton distribution is not considered in the analysis. A follow up to this investigation should include these double streaming protons.

[31] For a selected period, we tried to identify whether there is a correlation between measured minor ion densities (and their charge states) and the observed ε. We used iron and oxygen densities and charge states measured by SOHO/CELIAS/CTOF in 1996 (DOY 150–230) (See *Aellig et al.*

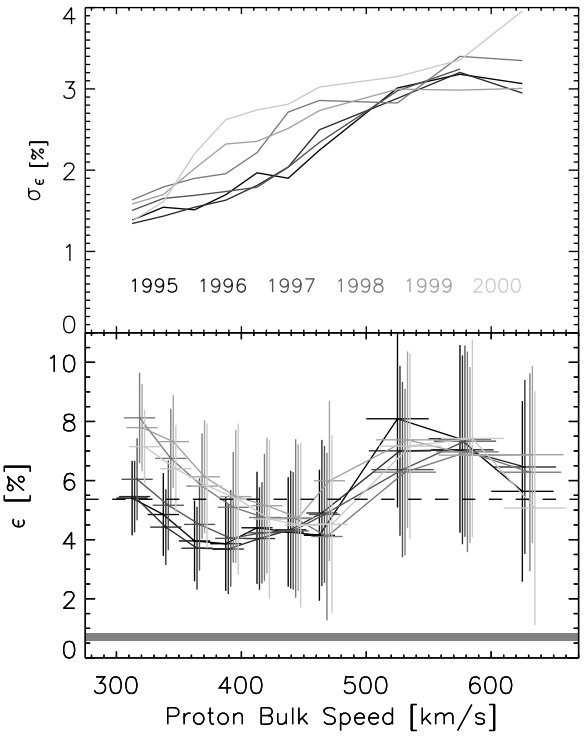

Figure 7. The center $\bar{\varepsilon}$ and width σ_ε of the best-fit Gaussians to the fractional excess ε of electron density unaccounted for by the solar wind hydrogen and helium for all years from 1995 to 2000 as a function of solar wind speed. The horizontal error bars for $\bar{\varepsilon}$ are the widths of the speed windows and the vertical error bars are the σ_ε. The expected contribution from minor ions (gray region from 0.8–1.5%) and the average value of $\bar{\varepsilon}$ = 5.4% (dashed line) are also shown. The higher values of $\bar{\varepsilon}$ and width σ_ε seen at speeds above 500 km/s may be due to the increased presence of proton beams. Accounting for minor ions, the typical difference between the FC and WAVES measurements is between 3 and 4.5%.

[1999] for details) with a time resolution of 5 min. On the basis of the relative abundances cited above, the low FIP (~10 eV and less) elements were tied to the observed iron density, while the high FIP elements were tied to the observed oxygen density. Assuming purely radial propagation, we compared these extrapolated densities and their electron contribution with the observed ε at Wind. The calculated time lags are well below 1 hour for the observation period mentioned. Correlations above 0.8 between the observed ε and Wind and the SOHO predictions have been found only if the following criteria were met simultaneously: (1) Restriction on DOY 150–170, when the lateral separation between SOHO and Wind was smallest, (2) averaging period of more than 1 day, (3) restriction to the speed window between 300 and 350 km/s. Furthermore, the correlation is strongly driven by periods with rather large values of ε. Excluding times with minor ion-associated electron number densities greater than 0.8/cc, the correlation decreases by more than 0.25 to about 0.55.

[32] Folding in the effects of minor ions, we have shown that the FC and TNR measurements of ion and electron number densities agree to within 3–4%. The difference is comparable with other effects, including the estimated accuracy of the TNR measurements, the speed-dependent σ_ε ranging from 1.5 to 3.5%, and the potential contribution to the total density from proton beams at high speeds. Other than a 1% difference in $\bar{\varepsilon}$ at low speeds between solar minimum and solar maximum, possibly due to a change in plasma composition, $\bar{\varepsilon}$ is stable over the interval studied, from 1995 through 2000. This is consistent with the stability of the FC measurement electronics as determined by the internal calibrations presented in Appendix B. Direct observations of hydrogen and helium number densities by an ion instrument may be combined with measurements of the electron plasma frequency to identify the consistency and stability of density measurements; for the Wind Faraday Cups and WAVES/TNR the agreement is to within several percent and stable over a decade timescale.

6. Conclusions

[33] We have examined the utility of three physics-based tests for identifying the uncertainty of solar wind ion measurements with observations from the Wind spacecraft serving as a case study. Two new techniques, using constraints of field-aligned differential flow and plasma microinstabilities to identify velocity and temperature measurement uncertainties, have been developed and applied in this paper for the first time. We have extended previous comparisons of ion number density and plasma frequency measurements by including the contribution of minor ions and by surveying the results as a function of time and solar wind speed.

[34] These methods have allowed us to characterize the uncertainty of solar wind ion parameters as measured by the Faraday Cups (FCs) on the Wind spacecraft. Modeling the breakdown of field alignment for small values of differential flow suggests velocity uncertainties are less than 0.16% in magnitude and 3° in direction. The persistence of measured temperature anisotropies at high beta implies an overall temperature uncertainty of 8%. This result suggests that the Wind FC measurements are effective for studying temperature anisotropies when the anisotropy exceeds 10%, which is to be expected for $\beta_{\|p} < 10$. A study of the FC internal calibration system presented in Appendix B demonstrates that the two FCs on Wind have remarkably small drifts in overall response of approximately 0.3% per decade. A yearly periodic variation in the response of 0.05%, due to variation in temperature of the electronics with distance from the Sun, is understood but much smaller than the measurement uncertainty of the density. Folding in the effects of minor ions, we identify a 3–4% speed-dependent offset between the FC ion densities and the WAVES/TNR plasma frequency-derived number density. The difference is greatest at high solar wind speeds, which we attribute to the presence of proton beams that are not analyzed in the ion data set used for this study. There is little variation in the difference over time except at the lowest solar wind speeds, which show a sudden 1% change in 1998. This could possibly be due to a compositional change in the solar wind minor ion composition entering solar maximum.

[35] These procedures are of general use and are applicable to observations from any solar wind ion instrument.

For the velocity and temperature techniques, the only requirement is measurements of the vector magnetic field. For the density, there must be measurements of the plasma frequency. We believe these quantitative studies of ion measurement uncertainties should be performed on any solar wind instrument that will be used to conduct rigorous plasma physics experiments and for heliospheric and planetary missions, where no companion spacecraft exists for intercalibration.

Appendix A: Analysis of a Single Ion Spectrum

[36] The FC has been a workhorse for space plasma measurements from the beginning of space exploration [*Vasylinuas*, 1971; *Gloeckler*, 1990]. The first observations of ion fluxes in space were performed using FCs with a large, fixed negative voltage to prevent the entrance of electrons into the detector [*Gringauz et al.*, 1960]. The performance and capabilities of FCs have been extended by reducing their mass and power requirements, [*Lazarus et al.*, 1993] and increasing their measurement cadence [*Aellig et al.*, 2001b]. Contrary to commonly held impressions, FCs not only provide measurements of the reduced distribution but in fact allow determination of the three-dimensional characteristics of ions in phase space such as differential flow [*Richardson*, 1986; *Clack et al.*, 2004] and temperature anisotropy [*Kasper et al.*, 2002].

[37] The operating principle of the twin Faraday Cup instruments on Wind, discussed by *Ogilvie et al.* [1995] is summarized here. Plasma enters the instrument through a large circular entrance aperture. In order to be detected, particles must have energy per change (E/q) sufficient to pass through a retarding grid. That retarding grid, also referred to as a modulator grid because a time-varying retarding potential is used, is sandwiched between two grounded grids. Thus transmitted particles are returned to their original incident energy. Farther along, particles encounter a 34 cm^2 circular limiting aperture that simplifies the calculation of the instrument response by removing effects of aberration near the modulator grid and defines the collecting area of the FC. Two semicircular metal collector plates detect the current produced by particles that pass through the limiting aperture. The collector plates are larger than the limiting aperture, so an incident cold particle beam falls entirely on the collector plate for angles of incidence of up to 45°; as a result, the FCs measure the reduced distribution function along a given line of sight. The large field of view of the FC permits a higher maximum measurable wind speed than may be expected, since the flow may be examined at high angles of incidence. In particular, though the maximum modulator voltage is only sufficient to stop normally incident protons up to 1200 km/s, the Wind FCs were able to observe speeds up to 1940 km/s during the unusual coronal mass ejection events of October 2003 [*Skoug et al.*, 2004].

[38] The voltage applied to the modulator grid alternates between two voltages at 200 Hz, leading transmitted particles to produce an alternating current on the collector plates. A measurement chain, AC-coupled to the collector plate, converts the current to a voltage and amplifies it. Because of the AC coupling the instrument is only sensitive to the current produced by ions within the E/q window being scanned. A demodulation circuit synchronized with the 200 Hz signal to the modulator inverts half of the resulting waveform to produce a constant positive voltage. This demodulated voltage is fed to an integrating circuit to average out noise followed by a logarithmic analog to digital conversion (log-ADC) of the integrated current into a digital number. The log-ADC covers the range from 10^{-13} A to 10^{-8} A with 1% resolution. The net effect of the modulator/demodulator is to make the measurement chain sensitive only to signals varying with the same frequency and proper phase relative to the modulator voltage. This process makes the FCs insensitive to photoelectrons produced by sunlight or to ionizing radiation produced by energetic particles. This insensitivity to ionizing radiation is especially important during intense solar energetic particle events such as the July 2000 Bastille Day coronal mass ejection [*Lepping et al.*, 2001]. Sweeping through a series of E/q windows at multiple azimuth angles as the spacecraft spins permits the FC to scan through phase space. Solar wind ion species such as hydrogen and helium separate in the E/q scan due to their different charge to mass ratios and the fact that they flow at similar speeds.

[39] A SWE FC spectrum consists of currents measured along 20 azimuth angles and 30 E/q windows by each of the two instruments. The exact number of energy windows depends on whether the FCs are tracking the peak of the proton distribution with fine energy resolution or scanning the full voltage range available to the modulator at half that resolution, but generally, a spectrum consists of 1200 currents.

[40] An impediment to comparing the solar wind parameters from different instruments is that different techniques are used to determine the set ($\vec{V}_j$, $w_{\perp j}$, $w_{\|j}$, n_j) that best describe the observations. For this study, we have applied the two techniques, a nonlinear fitting and summed moment method, to the SWE measurements. The resulting output of both methods is publicly available at the National Space Science Data Center. We prefer the fitting approach, in which we convolve the bi-Maxwellian distribution described above with the instrument response, predict the resulting currents, and then identify the values of the free parameters in the model that produce the best agreement with the observations. Strengths of the FC instrument are its straightforward response (with no energy dependence to the collecting efficiency) and the existence of analytic solutions for the current produced by an incoming Maxwellian or bi-Maxwellian distribution [*Kasper et al.*, 2002]. For a distribution function $f_j(\vec{v})$ such as the bi-Maxwellian defined in equation (1), the current dI due to an element in velocity space accessible to the collector plates is given by,

$$dI = Af(\vec{v})q\vec{v}\cdot\hat{n}d^3v, \tag{A1}$$

where A is the effective area of the FC, q is the charge of the species, and $\hat{n}$ is the look direction of the FC. The effective area is a function of the size of the limiting aperture and the transparencies of the wire grids within the instrument; it is only weakly dependent on the angle of incidence and we have found it sufficient to treat it as fixed. The total FC current ΔI due to the bi-Maxwellian in equation (1) is then given by integrating (A1) over all speeds perpendicular to $\hat{n}$

and within the speed window (V, $V + \Delta V$) along the line of sight,

$$\Delta I = \frac{An_j q_j}{\pi^{3/2} w_{\perp j}^2 w_{\|j}} \int_V^{V+\Delta V} \vec{v} \cdot \hat{n} e^{-v_\perp^2/w_{\perp j}^2 - v_\|^2/w_{\|j}^2} d^3v. \quad \text{(A2)}$$

The solution for ΔI is

$$\Delta I = \frac{An_j q}{2} \left[\frac{\tilde{w}}{\sqrt{\pi}} \left(e^{-\left(V_o - V_{zj}\right)^2/\tilde{w}^2} - e^{-\left(V_o + \Delta V - V_{zj}\right)^2/\tilde{w}^2} \right) + V_{zj} \left(erf \frac{V_o + \Delta V - V_{zj}}{\tilde{w}} - erf \frac{V_o - V_{zj}}{\tilde{w}} \right) \right], \quad \text{(A3)}$$

where $\tilde{w}$ is a combination of the two thermal speeds which is a function of the angle between along $\hat{n}$ and $\hat{b}$,

$$\tilde{w} = \sqrt{w_\|^2 \left(\hat{n} \cdot \hat{b} \right)^2 + w_\perp^2 \left(1 - \left(\hat{n} \cdot \hat{b} \right)^2 \right)}, \quad \text{(A4)}$$

and V_{zj} is the projection of the bulk velocity of the flow along $\hat{n}$.

[41] The optimum solution for ($\vec{V}_j$, $w_\perp j$, $w_{\|j}$, n_j) is identified by minimizing a χ^2 merit function, defined as the sum of the squared difference between the measured currents and those predicted by (A3), normalized by the uncertainty of the measurements. Instead of a Gaussian measurement uncertainty, we use the quantization error due to the 1% resolution of the log-ADC. We refer to this fitting process as the nonlinear technique because we employ the Levenberg-Marquardt nonlinear least-squares method to identify the minimum [*Press et al.*, 1999, section 15.5]. Figure A1 is an example of the best fit of the model response to a spectrum recorded on 29 February 2000, showing measurements along angles 17, 30, and 60 degrees relative to the local field. The final value of χ^2 indicates how well the selected observations are described by a bi-Maxwellian and is useful in identifying the presence of nonthermal features in the distribution such as proton beams and heat fluxes. For the analysis of hydrogen and helium, the predicted currents due to each species are summed and the χ^2 is minimized with respect to the 12 free parameters ($\vec{V}_p$, $w_{\perp p}$, $w_{\|p}$, n_p, $\vec{V}_\alpha$, $w_{\perp\alpha}$, $w_{\|\alpha}$, n_α).

[42] Once the minimum χ^2 is identified, a covariance matrix is calculated and inverted to yield estimates of the uncertainty of each of the best-fit parameters. Because the uncertainty we use in calculating χ^2 is not a Gaussian measurement error but the uncertainty due to the digital quantization error of the log-ADC, it is not obvious that the inversion yields Gaussian error estimates for the derived parameters. However, the error estimates do provide a qualitative aid for understanding systematic issues in the analysis of the FC spectra. As an example we consider how well the FC measurements constrain the parallel and perpendicular temperatures as a function of the orientation of the interplanetary magnetic field. Consider the implication of (A4) for determinations of the parallel and perpendicular thermal speeds. When $\hat{b} \parallel \hat{n}$, the reduced distribution function will have a width $\tilde{w} = w_\|$; likewise when $\hat{b} \perp \hat{n}$, the reduced distribution function will have a width $\tilde{w} = w_\perp$. The FC lines of sight are distributed within 15° of the ecliptic plane and clustered around the Sun-Earth line, so we expect a minimum in the error in $w_\|$ when $\vec{B}_o$ is radial. We define the angle ϕ_B of $\vec{B}_o$ in the ecliptic plane,

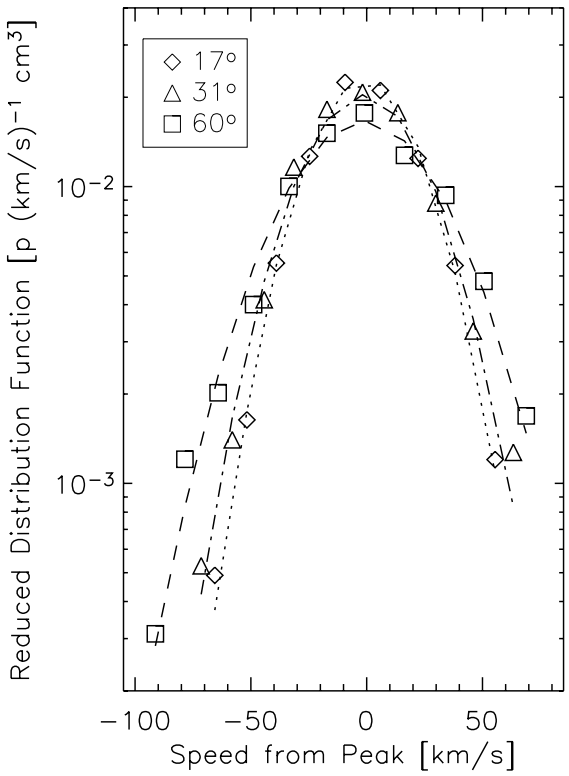

Figure A1. Example of nonlinear fit to determine plasma parameters for a spectrum recorded by the Wind FCs on 29 February 2000. The symbols are the measured reduced distribution function along three of the 40 angles in a single 92-s ion spectrum. The lines are the predicted values using the model response function. The legend indicates the average angle between the instrument and the magnetic field for each of the scans.

$$\phi_B \equiv \tan^{-1} \frac{B_y}{B_x} \quad \text{(A5)}$$

and θ_B as the angle of $\vec{B}_o$ out of the ecliptic plane,

$$\theta_B = \tan^{-1} \frac{B_z}{\sqrt{B_x^2 + B_y^2}}, \quad \text{(A6)}$$

where the components of $\vec{B}_o$ are in the Geocentric Solar Ecliptic (GSE) coordinate system. Figure A2 illustrates the systematic dependence of the uncertainty in $T_{\|p}$ and $T_{\perp p}$ as a function of the orientation of the interplanetary magnetic field. Figure A2a is a two-dimensional histogram of the distribution of ion spectra as a function of ϕ_B and θ_B and shows a strong clustering of measurements near $\phi_b \sim 135°$, the typical Parker spiral angle of the interplanetary magnetic field expected at Earth. The average percent uncertainty of the parallel and perpendicular temperatures is shown as a function of ϕ_B and θ_B in Figures A2b and A2c. The parallel temperature is most poorly constrained when the field is out

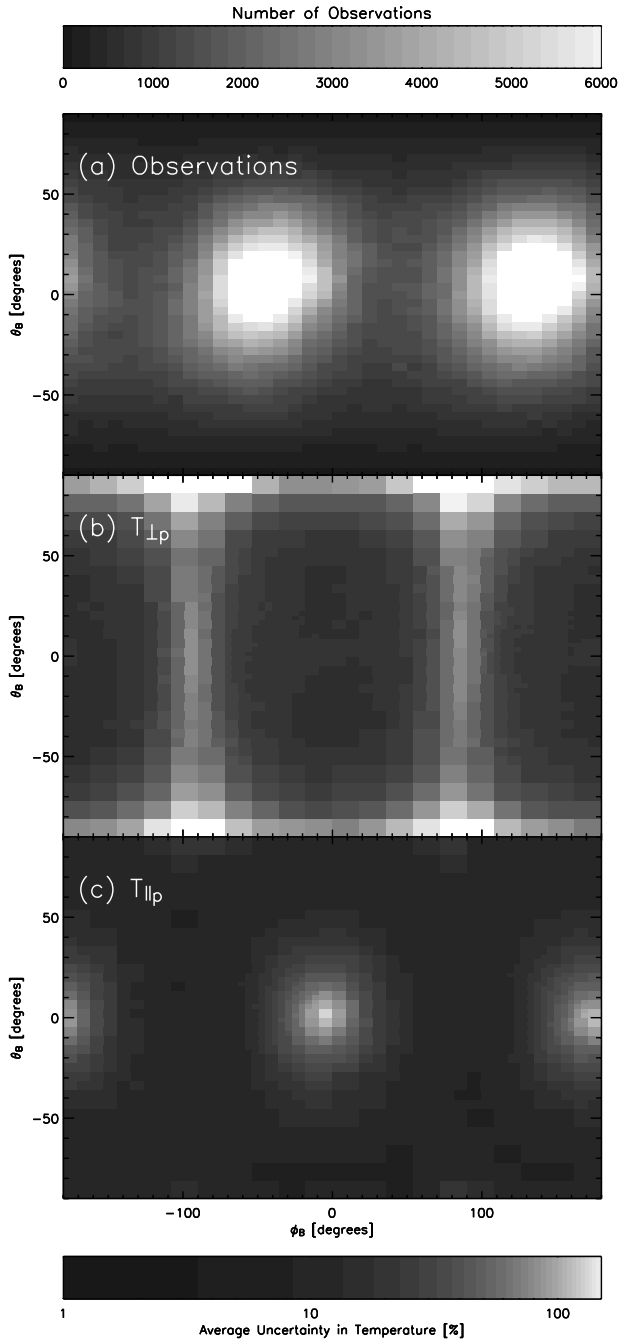

Figure A2. Demonstration of the dependence of the average uncertainty in best-fit derived temperatures on the orientation of the interplanetary magnetic field, where ϕ_B is the angle of the field in the ecliptic plane from the x-GSE axis, increasing toward the positive y-GSE axis, and θ_B is the angle out of the ecliptic plane, positive northward. (a) We show a two-dimensional histogram of the distribution of the magnetic field orientation using the average direction of $\hat{b}$ over each 92-s FC ion spectrum. The upper scale bar indicates the number of observations. (b) and (c) The average derived uncertainties in $T_{\|p}$ and $T_{\perp p}$, respectively, using shading indicated by the lower scale bar. The uncertainty in $T_{\|p}$ is a minimum when the field is in the ecliptic plane near the Sun-Earth axis, and the minima in the uncertainty in $T_{\perp p}$ occur when the field is out of the ecliptic plane or perpendicular to the Sun-Earth axis, as expected.

of the ecliptic plane or perpendicular to the Sun-Earth line. The perpendicular temperature is poorly constrained when the magnetic field is radial. The observed minima and maxima of the average uncertainties agrees with this picture, indicating that the derived uncertainties are at least indictors of configurations where the solar wind parameters are more poorly constrained. This suggests, for example, that statistical studies of temperature anisotropies with Wind FC data following the *Kasper et al.* [2002] analysis of the firehose instability should focus on measurements with the minimum estimated anisotropy uncertainty. Fortunately, the dominant Parker field orientation occurs at a near-optimum tradeoff between the uncertainties of the two component temperatures.

[43] A second method for deriving ion parameters from a spectrum is the moment technique, in which moment integrals of increasing order of the observed phase space density are approximated by various sums and then related to the density, velocity, and temperature. Consider the set of measurements $\Delta I_i(V_i, \Delta V_i)$ along one line of sight. On the basis of (A2), if we assume that the velocity distribution function varies slowly over the region of integration, and that the flux observed in that window are also from a single ion species, then the reduced distribution function $F_i(\vec{v})$ may be approximated as

$$F_i(\hat{n}) \cong \frac{\Delta I_i}{AqV_i\Delta V_i}. \tag{A7}$$

The density is then just

$$n(\hat{n}) \simeq \sum_i F_i \Delta V_i \tag{A8}$$

The bulk speed projected along each angle is

$$V(\hat{n}) \simeq \frac{1}{n}\sum_i V_i F_i \Delta V_i \tag{A9}$$

and the projected thermal speed is

$$\tilde{w}(\hat{n})^2 \simeq \frac{1}{n}\sum_i F_i \Delta V_i \left(V_i - V_p\right)^2 \tag{A10}$$

[44] The projected speeds as a function of angle are inverted to determine the bulk velocity of the protons. Since we see from (A4) that the effective thermal speed is a combination of $w_{\perp}p$ and $w_{\|p}$ as a function of $\hat{b} \cdot \hat{n}$, the thermal speed measurements may also be inverted. Figure A3 provides examples of the moment determination of density and temperatures for the same spectrum shown in Figure A1. The upper panel shows the value of n_p derived along each line of sight as a function of the angle between the FC and the solar wind flow. Once the flow exceeds 45 degrees, the effective collecting area of the FC rapidly drops, leading to an underestimate of n_p; Lines of sight with angles exceeding 35° are discarded from the moment analysis. The second panel is a plot of measured thermal speed as a function of the angle between the line of sight and $\vec{B}_o$. The dashed line is the best fit of the effective thermal speed as predicted by (A4). In this example, the

derived temperatures agreed within several percent between the moment and nonlinear methods.

[45] Table A1 is a summary of the typical error estimate from the nonlinear fitting and the difference between the moment and nonlinear analysis techniques for several solar wind parameters. We note that there is generally a good agreement between the two techniques, except in the case of temperatures. Numerical simulations suggest that this difference is due to contamination of the moment analysis by helium and non-Maxwellian aspects of the proton distribution such as beams [*Kasper*, 2003]. It is important to note that we did not take great care in writing a moment analysis algorithm that was insensitive to these effects, since the nonlinear analysis is our final science product and the moments function more as a diagnostic. Also, while Figure 3 illustrates that the uncertainty estimates from the nonlinear fits produce sensible systematic variations, we must be skeptical about the absolute values. For example, consider the average uncertainties in the N/S and E/W flow angles, which are unbelievably small. This highlights the need for the physics-based tests to identify uncertainty in velocity, temperature, and density presented within this paper.

Table A1. Comparison of Nonlinear and Moment Results[a]

Parameter	Estimate of Uncertainty From Nonlinear Fit	Deviation of Difference Between Moment and Nonlinear
Bulk speed	3.6%	0.5%
East-West flow angle	0.04°	0.4°
North-South flow angle	0.01°	0.2°
Perpendicular temperature	8.3%	23%
Parallel temperature	6.6%	23%
Density	0.8%	2.8%

[a]The average uncertainty in each parameter as derived from the nonlinear fit is listed in the second column. The third column is the standard deviation of the difference between the nonlinear and moment results.

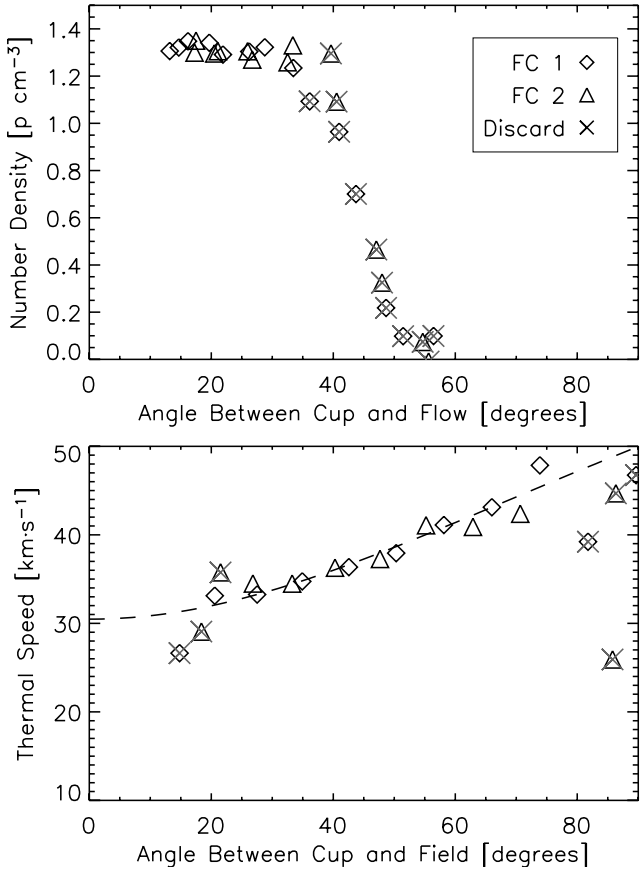

Figure A3. A demonstration of the determination of proton density and temperature anisotropy with the moment method, for the same spectrum shown in Figure A1. The proton number densities determined by each cup are shown in the upper plot, with diamonds for FC1 and triangles for FC2, as a function of the angle between the FCs and the solar wind flow. When the angle between the cup and the flow exceeds 35°, a fraction of the solar wind flow is unable to enter the instrument and the derived density and temperature decreases. These points are marked with an "x" and discarded from the subsequent analysis. The lower plot shows the moment thermal speed as a function of the angle between the FCs and the local field, along with the best-fit of equation (A4). In this case the perpendicular temperature is nearly three times the parallel temperature, in close agreement with the best-fit result.

Appendix B: Faraday Cup Instrument Stability

[46] In this appendix we discuss the stability of the FC hardware and electronics. In general, the factors that lead to long-term instrument degradation can be separated into two categories: changes in the particle sensor/detector and changes in analog measurement circuitry. A common example of detector evolution is the gain degradation of solid-state solar wind detectors due to lifetime radiation dosage in space. While the metal FC collector plates are not sensitive to radiation damage, great care is taken to ensure the stability of the collection surface. The collector plates are fabricated from magnesium to reduce mass but to prevent oxidation of the magnesium the plates have an external coating of gold. Gold ions can slowly diffuse into magnesium, with more rapid diffusion rates for temperatures exceeding 400 K [*Toukan et al.*, 1997]. The magnesium plates were coated with a flash of copper followed by a nickel shield before the final layer of gold was deposited. A special electrolytic process was employed when depositing the nickel to prevent the formation of large crystal domains, thus limiting the magnetic susceptibility of the collectors and the resulting effect on the MFI instrument. Because of this design, the efficiency of the collector plates is not expected to evolve on timescales of decades.

[47] We next consider the possible long-term changes in the analogue measurement circuitry. Components such as reference voltages, amplifiers, and resistors were selected with long-term stability in mind, with estimates for total drift over the mission of about one part per thousand. Each FC has an internal calibration system capable of producing any of 12 logarithmically spaced currents from 10^{-13} to 10^{-8} amps and injecting them into the measurement chain. The calibration currents are produced with a single reference voltage source and a resistor-divider ladder. Smaller currents are produced farther down the ladder. We can generally distinguish between changes in the calibration system and the analog measurement chain by examining

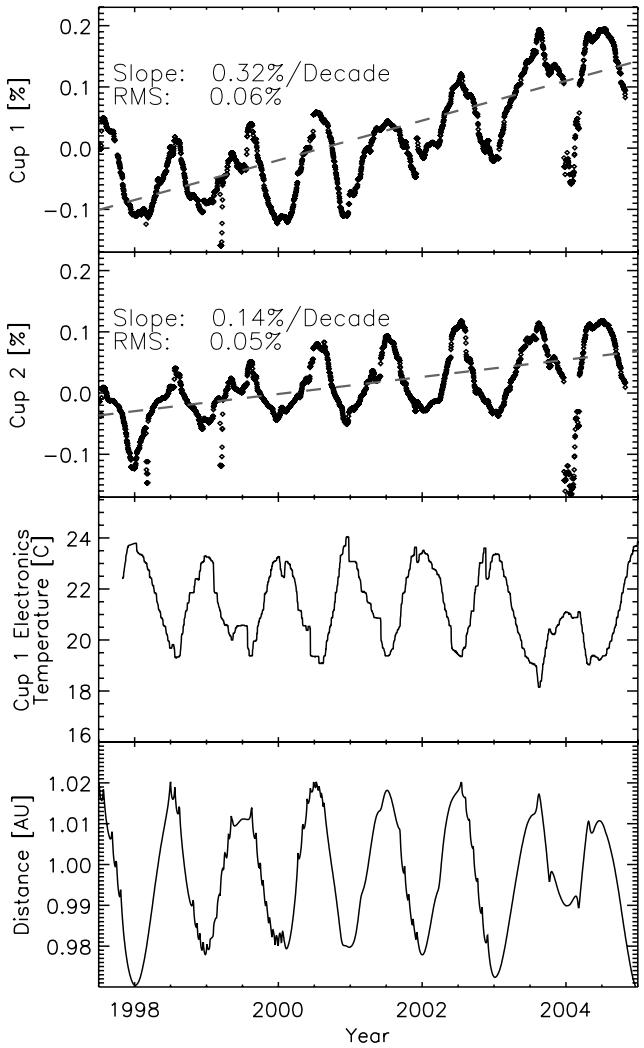

Figure B1. Stability of the response of the Faraday Cups on Wind over time. The top two panels show the percent change in response to a 10^{-11} A internal calibration signal over the last 6 years of the mission. The dashed lines are the best fit of a line to the change with time, yielding trends of 0.32% and 0.15% per decade for the two cups. The RMS variation of the instrument responses about the linear trend is about 0.05% for both cups. This periodic variation is correlated with changes in the electronics temperatures (third panel) due to the variation of the distance of the spacecraft from the Sun (fourth panel). The magnitude of the change and the direction of the temperature dependence are consistent with the expected performance of the log ADC.

trends in all 12 calibration currents. The calibration system cycles through these currents every 18 minutes injecting one current during a 3-s interval preceding the start of each spectrum. The FC internal calibrators have operated continuously since launch, so we can quantify the stability of the response of the measurement chains by examining the variation of the currents measured during the calibration sequences.

[48] In order to evaluate the long-term stability of the FC electronics, we calculated daily averages of the measured current for each of the 12 injection currents on each FC. For injection currents greater than 10^{-10} A it is rare to see the measured current change; in other words any variation is less than the 1% quantization of the log-ADC. Variation is seen with the smaller injected currents, and a typical example is shown in Figure B1. The top two panels of Figure B1 show the daily average of the percent change in the response of the two FCs to a 10^{-11} A calibration signal (typical solar wind currents are in the range of 10^{-11} to 10^{-9} A). The third panel of the figure is the temperature of the box that houses the electronics for FC1. An annual modulation of the calibration signal with rms amplitude of 0.05% is anticorrelated with variation in the temperature of the electronics box. These periodic temperature variations are simply due to the radial distance of Earth from the Sun as shown in the final panel of the figure. The amplitude and direction of the change and the fact that this modulation is only seen for small currents, is consistent with the variation induced by the temperature dependence of a capacitor in the log-ADC system. The dashed lines in these plots are the best-fit line through the change, which yield an overall variation of 0.25% per decade and 0.07% per decade for the two instruments. This demonstrates the remarkable stability of these Faraday Cups; neither the annual variation nor the long-term drift over a decade are great enough to affect the derived solar wind parameters.

[49] **Acknowledgments.** Analysis of the Wind SWE Faraday Cup data is supported by NASA grant NAG-10915. The authors thank Thomas Zurbuchen, Sue Lepri, and Jim Raines for discussions of minor ion composition and charge state and for the 2004 ACE SWICS data sets, and Jean-Louis Bougeret, Milan Maksimovic, Chadi Salem, and the CDPP (Centre de Donnees en Physique des Plasmas) for access to the TNR measurements and discussions of the analysis. The authors also thank the reviewers for their helpful comments and suggestions.

[50] Shadia Rifai Habbal thanks Milan Maksimovic and Susan T Lepri for their assistance in evaluating this paper.

References

Aellig, M. R., S. Hefti, H. Grunwaldt, P. Bochsler, P. Wurz, F. M. Ipavich, and D. Hovestadt (1999), The Fe/O elemental abundance ratio in the solar wind as observed with SOHO/CELIAS/CTOF, *J. Geophys. Res.*, *104*, 24,769.

Aellig, M. R., A. J. Lazarus, J. C. Kasper, and K. W. Ogilvie (2001a), Rapid measurements of solar wind ions with the Triana PlasMag Faraday Cup, *Astrophys. Space Sci.*, *277*, 305.

Aellig, M. R., A. J. Lazarus, and J. T. Steinberg (2001b), The solar wind helium abundance: Variation with wind speed and the solar cycle, *Geophys. Res. Lett.*, *28*, 2767.

Anderson, B. J., S. A. Fuselier, S. P. Gary, and R. E. Denton (1994), Magnetic spectral signatures in the Earth's magnetosheath and plasma depletion layer, *J. Geophys. Res.*, *99*, 5877.

Anderson, B. J., R. E. Denton, G. Ho, D. C. Hamilton, S. A. Fuselier, and R. J. Strangeway (1996), Observational test of local proton cyclotron instability in the Earth's magnetosphere, *J. Geophys. Res.*, *101*, 21,527.

Araneda, J. A., A. F. Vinas, and H. F. Astudillo (2002), Proton core temperature effects on the relative drift and anisotropy evolution of the ion beam instability in the fast solar wind, *J. Geophys. Res.*, *107*(A12), 1453, doi:10.1029/2002JA009337.

Bougeret, J.-L., et al. (1995), WAVES: The Radio and Plasma Wave Investigation on the Wind spacecraft, *Space Sci. Rev.*, *71*, 231.

Clack, D., A. J. Lazarus, and J. C. Kasper (2002), A statistical study of proton double streaming observed by Wind/SWE, *Eos Trans. AGU*, *83*(19), Spring Meet. Suppl., Abstract SH21C-07.

Clack, D., J. C. Kasper, A. J. Lazarus, J. T. Steinberg, and W. M. Farrell (2004), Wind observations of extreme ion temperature anisotropies in the lunar wake, *Geophys. Res. Lett.*, *31*, L06812, doi:10.1029/2003GL018298.

Dusenbery, P. B., and J. V. Hollweg (1981), Ion-cyclotron heating and acceleration of solar wind minor ions, *J. Geophys. Res.*, *86*, 153.

Eviatar, A., and M. Schulz (1970), Ion-temperature anisotropies and the structure of the solar wind, *Planet Space Sci.*, *18*, 321.

Gary, S. P., H. Li, S. O'Rourke, and D. Winske (1998), Proton resonant firehose instability: Temperature anisotropy and fluctuating field constraints, *J. Geophys. Res.*, *103*, 14,567.

Gary, S. P., L. Yin, and D. Winske (2000), Electromagnetic proton cyclotron anisotropy instability: Wave-particle scattering rate, *Geophys. Res. Lett.*, *27*, 2457.

Gary, S. P., R. M. Skoug, J. T. Steinberg, and C. W. Smith (2001), Proton temperature anisotropy constraint in the solar wind: ACE observations, *Geophys. Res. Lett.*, *28*, 2759.

Gloeckler, G. (1990), Ion composition measurement techniques for space plasmas, *Rev. Sci. Instrum.*, *61*, 3613.

Gringauz, K. I., V. V. Bezrukikh, V. D. Ozerov, and R. E. Rybchinskii (1960), A study of the interplanetary ionized gas, high-energy electrons, and corpuscular radiation from the Sun by means of the three-electrode trap for charged particles on the second Soviet cosmic rocket, *Dokl. Akad. Nauk. SSSR*, *131*, 1301.

Hefti, S., H. Gruenwaldt, P. Bochsler, and M. R. Aellig (2000), Oxygen freeze-in temperatures measured with SOHO/CELIAS/CTOF, *J. Geophys. Res.*, *105*, 10,527.

Issautier, K., R. M. Skoug, J. T. Gosling, S. P. Gary, and D. J. McComas (2001), Solar wind plasma parameters on Ulysses: Detailed comparison between the URAP and SWOOPS experiments, *J. Geophys. Res.*, *106*, 15,665.

Kasper, J. C. (2003), Solar wind plasma: Kinetic properties and microinstabilities, Ph.D. thesis, Mass. Inst. of Technol., Cambridge, Mass.

Kasper, J. C., A. J. Lazarus, and S. P. Gary (2002), Wind/SWE observations of firehose constraint on solar wind proton temperature anisotropy, *Geophys. Res. Lett.*, *29*(17), 1839, doi:10.1029/2002GL015128.

Kasper, J. C., A. J. Lazarus, S. P. Gary, and A. Szabo (2003), Solar wind temperature anisotropies, in *Solar Wind 10*, edited by M. Velli, R. Bruno, and F. Malara, *AIP Conf. Proc.*, *679*, 538–541.

King, J. H., and N. E. Papitashvili (2005), Solar wind spatial scales in and comparisons of hourly Wind and ACE plasma and magnetic field data, *J. Geophys. Res.*, *110*, A02104, doi:10.1029/2004JA010649.

Lazarus, A. J., J. T. Steinberg, and R. L. McNutt (1993), A low-mass Faraday Cup experiment for the solar wind, in *Small Instruments for Space Physics: Proceedings of the Small Instrument Workshop Held 29–31 March, 1993 in Pasadena, CA*, edited by B. T. Tsurutani, sect. 3, pp. 3–11, Space Phys. Div., NASA, Washington, D. C.

Lepping, R. P., et al. (1995), The Wind Magnetic Field Investigation, *Space Sci. Rev.*, *71*, 207.

Lepping, R. P., et al. (2001), The Bastille Day magnetic clouds and upstream shocks: Near-Earth interplanetary observations, *Solar Phys.*, *204*, 285.

Maksimovic, M., S. Hoang, N. Meyer-Vernet, M. Moncuquet, J. L. Bougeret, J. L. Phillips, and P. Canu (1995), Solar wind electron parameters from quasi-thermal noise spectroscopy and comparison with other measurements on Ulysses, *J. Geophys. Res.*, *100*, 19,881.

Maksimovic, M., J.-L. Bougeret, C. Perche, J. T. Steinberg, A. J. Lazarus, A. F. Vinas, and R. J. Fitzenreiter (1998), Solar wind density intercomparisons on the Wind spacecraft using WAVES and SWE experiments, *Geophys. Res. Lett.*, *25*, 1265.

Marsch, E., H. Rosenbauer, R. Schwenn, K.-H. Muehlhaeuser, and F. M. Neubauer (1982a), Solar wind helium ions: Observations of the HELIOS solar probes between 0.3 and 1 AU, *J. Geophys. Res.*, *87*, 35.

Marsch, E., R. Schwenn, H. Rosenbauer, K.-H. Muehlhaeuser, W. Pilipp, and F. M. Neubauer (1982b), Solar wind protons: Three-dimensional velocity distributions and derived plasma parameters measured between 0.3 and 1 AU, *J. Geophys. Res.*, *87*, 52.

McKenzie, J. F., W.-H. Ip, and W. I. Axford (1978), Anomalous acceleration of minor ions in the solar wind, *Nature*, *274*, 351.

Meyer-Vernet, N., and C. Perche (1989), Tool kit for antennae and thermal noise near the plasma frequency, *J. Geophys. Res.*, *94*, 2405.

Neubauer, M. (1976), The role of Coulomb collisions in limiting differential flow and temperature differences in the solar wind, *J. Geophys. Res.*, *81*, 78.

Ogilvie, K. W., et al. (1995), SWE, A comprehensive plasma instrument for the Wind spacecraft, *Space Sci. Rev.*, *71*, 55.

Parker, E. N. (1958), Dynamical instability in an anisotropic ionized gas of low density, *Phys. Rev.*, *109*, 1874.

Paularena, K. I., and A. J. Lazarus (1994), Comment on "Intercalibration of solar wind instruments during the International Magnetospheric Study" by S. M. Petrinec and C. T. Russell, *J. Geophys. Res.*, *99*, 14,777.

Petrinec, S. M., and C. T. Russell (1993), Intercalibration of solar wind instruments during the international magnetospheric study, *J. Geophys. Res.*, *98*, 18,963.

Phan, T.-D., G. Paschmann, W. Baumjohann, N. Sckopke, and H. Luehr (1994), The magnetosheath region adjacent to the dayside magnetopause: AMPTE/IRM observations, *J. Geophys. Res.*, *99*, 121.

Press, W. H., S. A. Teukolsky, W. T. Vetterling, and B. P. Flannery (1999), *Numerical Recipes in C: The Art of Scientific Computing*, 2nd ed., Cambridge Univ. Press, New York.

Richardson, J. D. (1986), Thermal ions at Saturn: Plasma parameters and implications, *J. Geophys. Res.*, *91*, 1381.

Salem, C., J.-M. Bosqued, D. E. Larson, A. Mangeney, M. Maksimovic, C. Perche, R. P. Lin, and J.-L. Bougeret (2001), Determination of accurate solar wind electron parameters using particle detectors and radio wave receivers, *J. Geophys. Res.*, *106*, 21,701.

Scime, E. E., P. A. Keiter, M. M. Balkey, R. F. Boivin, J. L. Kline, M. Blackburn, and S. P. Gary (2000), Ion temperature anisotropy limitation in high beta plasmas, *Phys. Plasmas*, *7*, 215.

Shafer, C. M., G. Gloeckler, A. B. Galvin, F. M. Ipavich, J. Geiss, R. von Steiger, and K. Ogilvie (1993), Sulfur abundances in the solar wind measured by SWICS on Ulysses, *Adv. Space Res.*, *13*, 79.

Skoug, R. M., J. T. Gosling, J. T. Steinberg, D. J. McComas, C. W. Smith, N. F. Ness, Q. Hu, and L. F. Burlaga (2004), Extremely high speed solar wind: 29–30 October 2003, *J. Geophys. Res.*, *109*, A09102, doi:10.1029/2004JA010494.

Steinberg, J. T., A. J. Lazarus, K. W. Ogilvie, R. Lepping, and J. Byrnes (1996), Differential flow between solar wind protons and alpha particles: First Wind observations, *Geophys. Res. Lett.*, *23*, 1183.

Tan, L. C., S. F. Fung, R. L. Kessel, S.-H. Chen, J. L. Green, and T. E. Eastman (1998), Ion temperature anisotropies in the Earth's high-latitude magnetosheath: Hawkeye observations, *Geophys. Res. Lett.*, *25*, 587.

Toukan, K., I. Khubeis, F. Al-Zubi, M. Al-Sa'adi, S. Dababneh, E. Bakraji, and O. Meyer (1997), Diffusion behaviour of gold and mercury implanted into magnesium, *Nucl. Instrum. Meth. B*, *127*, 747.

Tu, C.-Y., L.-H. Wang, and E. Marsch (2003), A possible way of understanding the differential motion of minor ions in the solar wind, *J. Geophys. Res.*, *108*(A4), 1161, doi:10.1029/2002JA009561.

Vasylinuas, V. M. (1971), Deep space plasma measurements, in *Methods of Experimental Physics*, vol. 98, pp. 49–88, Elsevier, New York.

von Steiger, R. (1995), Composition of the solar wind, habilitation thesis, Univ. of Bern, Bern, Switzerland.

von Steiger, R., J. Geiss, G. Gloeckler, and A. B. Galvin (1995), Kinetic properties of heavy ions in the solar wind from SWICS/Ulysses, *Space Sci. Rev.*, *72*, 71.

Xing, L., and S. R. Habbal (2000), Proton/alpha magnetosonic instability in the fast solar wind, *J. Geophys. Res.*, *105*, 7583.

J. C. Kasper and A. J. Lazarus, MIT Kavli Institute for Astrophysics and Space Research, Massachusetts Institute of Technology, Building 37-673, 77 Massachusetts Avenue, Cambridge, MA 02139, USA. (jck@mit.edu)

K. W. Ogilvie and A. Szabo, NASA Goddard Space Flight Center, Greenbelt, MD 20771, USA.

J. T. Steinberg, Space Science and Applications (ISR-1), Los Alamos National Laboratory, Mail Stop D466, Los Alamos, NM 87545, USA.